Acta Cryst. (1998). B**54**, 750–765

Atomic Structure of $PbZrO_3$ Determined by Pulsed Neutron Diffraction

S. Teslic† and T. Egami*

Department of Materials Science and Engineering and Laboratory for Research on the Structure of Matter, University of Pennsylvania, Philadelphia, PA 19104-6272, USA. E-mail: egami@seas.upenn.edu

(*Received 21 January 1997; accepted 6 March 1998*)

Abstract

The atomic structure of lead zirconate, $PbZrO_3$ (PZ), was studied using Rietveld refinement and atomic pair distribution function analysis of pulsed neutron powder diffraction data for the antiferroelectric, intermediate and paraelectric phases. The symmetry of PZ at $T = 20$ K in the antiferroelectric phase was determined to be *Pbam*. The structure was characterized by distortions of the ZrO_6 octahedra which are smaller than in previous studies. Locally correlated displacements of Pb in the *c* direction develop with increasing temperature. The average magnitude was 0.06 Å at room temperature, 0.14 Å at $T = 473$ K and 0.20 Å in the intermediate phase at $T = 508$ K. The intermediate phase was characterized by in-plane antiferroelectric Pb displacements which produce $\frac{1}{2}\{110\}$ superlattice diffraction peaks. Above 473 K the local structure of PZ remains largely unchanged, in spite of the transitions in the long-range order from the antiferroelectric to the intermediate and to the paraelectric phases.

1. Introduction

Lead zirconate ($PbZrO_3$, PZ) is an end member of the solid-solution oxides $PbZr_{1-x}Ti_xO_3$ (PZT), which are technologically important for their ferroelectricity and piezoelectricity observed over a wide range of compositions. PZ is also perhaps the best known and most frequently studied case of antiferroelectricity in perovskites. Nevertheless, there have been controversies in the literature for some time regarding its dielectric properties and atomic structure. The first complete structural analysis using single-crystal X-ray and powder neutron diffraction was made by Jona *et al.* (1951), hereinafter referred to as JSMP. They observed antiparallel $[1\bar{1}0]$ Pb displacements and oxygen octahedra rotations around the $[1\bar{1}0]$ axis in the pseudocubic lattice. The neutron diffraction profile refinement indicated unbalanced oxygen shifts along the *c* direction. Their choice of non-centrosymmetric *Pba*2 symmetry of the antiferroelectric (AFE) phase appeared to be consistent with the observation of weak piezoelectricity by Roberts (1949). However, in order to observe this effect, Roberts (1949) polarized a ceramic disc by applying d.c. or pulsed electric fields while cooling from $T = 523$ to 373 K through the phase transition. By contrast, Scott & Burns (1972) found no piezoelectric effect in single crystals.

Under these circumstances, it was necessary to examine critically the choice between *Pba*2 and *Pbam*. The subsequent powder neutron diffraction profile analysis of PZ by Fujishita *et al.* (1982), hereinafter referred to as FSAS, gave a better reliability factor for *Pbam* than for *Pba*2 symmetry. FSAS refined balanced oxygen displacements along the *c* direction, resulting in no local polarization. Following this, Tanaka *et al.* (1982*a*,*b*) also suggested *Pbam* symmetry and determined the oxygen coordinates using electron diffraction techniques. However, more recently, Dai *et al.* (1995) performed polarization measurements which show a very small reversible spontaneous polarization along the *c* direction. At the same time, no evidence of second-phase formation or the presence of local ferroelectric (FE) domains was found by extensively examining the PZ sample using transmission electron microscopy (TEM) and selected-area electron diffraction techniques (Dai *et al.*, 1995). Thus, questions regarding the existence of polarization and the nature of the atomic structure of PZ are still open. It is interesting to note that a recent total electron energy calculation using the local density approximation (LDA) demonstrated the coexistence of both FE and AFE instabilities in PZ, with a very delicate balance between them (Singh, 1995).

Early experiments on PZ reported only one phase transition at around $T = 520$ K between the low-temperature AFE phase and the high-temperature paraelectric (PE) phase. However, the existence of a narrow intermediate phase was established later, although its nature and atomic structure are still controversial (Fujishita & Hoshino, 1984; Whatmore & Glazer, 1979). The intermediate phase was suggested to be an FE phase by X-ray structural analysis (Tennery, 1966; Goulpeau, 1966), dielectric (Shirane *et al.*, 1951) and Raman studies (Roleder *et al.*, 1988). On the other hand, Fujishita & Hoshino (1984) identified the intermediate phase as an AFE phase. It is now known that

† Present address: Materials Science Division, Argonne National Laboratory, Argonne, IL 60439-4814, USA.

ISSN 0108-7681

the two phase transitions around 520 K involve condensation of at least four soft modes, which may interact in a very complicated way (Fujishita & Hoshino, 1984; Cochran & Zia, 1968).

The purpose of the current work is to investigate once again the atomic structure of PZ as a function of temperature using new tools of structural study. We used both the Rietveld refinement method and atomic pair distribution function (PDF) analysis of pulsed neutron powder diffraction data to study the atomic structure of PZ. The Rietveld reciprocal-space refinement of powder diffraction data provides the long-range average structure. On the other hand, 'real-space' refinement of the PDF reveals local and intermediate structural information which is not explicitly reflected in the long-range structure (Egami, 1995). In fact, a 'real-space' refinement of the PDF and a 'reciprocal-space' (or Rietveld) refinement of the diffraction data provide highly complementary information. We used combined PDF and Rietveld analysis to obtain a complete picture of the atomic structure, both in the short range as well as in the long range.

2. Sample preparation and experimental procedure

A powder sample of $PbZrO_3$ was prepared by a conventional mixed oxide method by the group of Professor D. Viehland of the University of Illinois. PZ ceramics were derived from high purity (> 99.9%) starting oxides of PbO and ZrO_2. Powders were weighed and mixed using yttrium-stabilized ZrO_2 media in deionized water for 12 h. The slurry was dried at 371 K and calcined at 1123 K for 4 h. The calcined powder was then size reduced to a submicron consistency in a ball mill using zirconia in deionized water for 12 h and dried overnight at 423 K. No evidence of impurity phases could be seen in the X-ray or neutron diffraction patterns.

Neutron diffraction patterns were measured for the PZ sample using the Special Environment Powder Diffractometer (SEPD) at the Intense Pulsed Neutron Source (IPNS) of the Argonne National Laboratory (Jorgensen *et al.*, 1989). Data were collected using the time-of-flight method with no energy discrimination at the detector. The sample, weighing 14.53 g, was sealed in a vanadium sample holder with He-exchange gas and cooled using a Displex closed-loop He refrigerator for low-temperature measurements. Data were collected at T = 20, 100, 150, 200 and 300 K. For high-temperature measurements the sample was sealed in a vanadium holder and heated using a vanadium furnace, and data were collected at T = 300, 473, 508 and 523 K. The duration of each run was approximately 4 h per temperature. Diffraction patterns were first analyzed by the Rietveld method using the IPNS Rietveld package (Von Dreele *et al.*, 1982) over the d range 0.5–4.0 Å. Although data were collected on five detector banks, all of which were used in the PDF analysis, only the high-resolution 90° bank data ($\Delta d/d$ = 0.006) were analyzed in the Rietveld refinement. The background was modeled using a polynomial function and subtracted from the diffraction pattern. Diffraction peaks were described using a two-sided exponential function that was convoluted with a Gaussian to describe the instrumental and sample contributions to the peak profile, respectively. The scattering lengths used in the refinement were: Pb 0.940, Zr 0.716, O 0.580 $\times 10^{-12}$ cm. The overall scale factor, parameters defining peak shapes, counter-zero error, atomic position parameters, isotropic thermal (atomic displacement) factors and unit-cell parameters were refined. The Rietveld-refined weighted profile reliability factor, R_{wp}, which is used throughout the text, is defined in the usual manner (Von Dreele *et al.*, 1982). Initial refinements suggested that the site occupancy was 100% and this value was fixed on all sites. As an example the 20 K data and their refinement are shown in Fig. 1.

3. Crystallographic structure of PZ

3.1. *Low-temperature phase*

The 20 K and room-temperature data were subjected to Rietveld analysis in order to resolve the confusion in the symmetry and atomic positions in the AFE phase. After preliminary refinements to establish the scale factor and the peak-shape parameters we refined the unit-cell parameters, atomic positions and thermal factors in the non-centrosymmetric *Pba*2 and centrosymmetric *Pbam* symmetries. The refinement in *Pba*2 symmetry resulted in an R_{wp} factor of 0.0805, while in *Pbam* symmetry the R_{wp} factor converged to 0.0727. Since *Pba*2 is a subgroup of *Pbam*, the parameters refined in *Pbam* symmetry are also acceptable in *Pba*2. Thus, ideally the refinement in *Pba*2 symmetry should

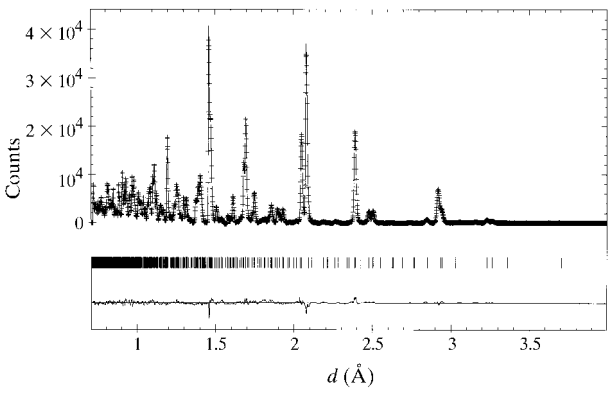

Fig. 1. An example of a result of the Rietveld refinement for the PZ data collected at T = 20 K. The solid line is the calculated profile. The tick marks below the profile indicate the positions of the allowed diffraction peaks. The difference plot (observed minus calculated) is shown at the bottom. The fitted background has been subtracted before plotting.

Table 1. *Rietveld-refined structural parameters from the data in space group Pbam at T = 20 K and room temperature, and proposed by Fujishita et al. (1992)*

The goodness-of-fit (S) agreement index is defined as R_{wp}/R_e where R_e is the expected value of the R factor for perfect fitting. The primed and non-primed atomic positions are located in the top and bottom blocks of the unit cell.

	x	y	z	B
20 K				
Pb	0.697 (2)	0.123 (2)	0.0	0.25 (3)
Pb′	0.707 (2)	0.125 (2)	0.5	0.25 (3)
Zr	0.240 (1)	0.125 (1)	0.25	0.03 (2)
Zr′	(0.240	0.125	0.750)	0.03 (2)
O1	0.276 (2)	0.151 (1)	0.0	0.05 (3)
O1′	0.298 (2)	0.088 (1)	0.5	0.05 (3)
O2	0.032 (2)	0.262 (2)	0.277 (3)	0.44 (2)
O2′	(0.032	0.262	0.723)	0.44 (2)
O3	0.0	0.5	0.200 (2)	0.27 (2)
O3′	(0.0	0.5	0.800)	0.27 (2)
O4	0.0	0.0	0.228 (2)	0.17 (2)
O4′	(0.0	0.0	0.772)	0.17 (2)
Dimensions (Å)	5.8822 (4), 11.7813 (6), 8.2293 (4)			
R_{wp}	0.0727			
S	3.69			
Room temperature				
Pb	0.704 (2)	0.124 (2)	0.0	1.15 (3)
Pb′	0.709 (2)	0.128	0.5	1.15 (3)
Zr	0.240 (2)	0.126 (1)	0.25	0.17 (3)
Zr′	(0.240	0.126	0.75)	0.17 (3)
O1	0.272 (2)	0.148 (1)	0.0	0.34 (4)
O1′	0.295 (2)	0.088 (1)	0.5	0.34 (4)
O2	0.030	0.262 (2)	0.275 (3)	0.80 (3)
O2′	(0.030	0.262	0.725)	0.80 (3)
O3	0.0	0.5	0.202 (2)	0.67 (3)
O3′	(0.0	0.5	0.798)	0.67 (3)
O4	0.0	0.230 (3)	0.90 (2)	
O4′	(0.0	0.0	0.770)	0.90 (2)
Dimensions (Å)	5.8819 (4), 11.7820 (6), 8.2294 (6)			
R_{wp}	0.0688			
S	3.48			
Fujishita *et al.* (1982)				
Pb	0.706 (2)	0.127 (2)	0.0	1.01 (2)
Pb′	(0.706	0.127	0.5)	1.01 (2)
Zr	0.242 (3)	0.125 (1)	0.25	0.20 (3)
Zr′	(0.242	0.125	0.75)	0.20 (3)
O1	0.271 (3)	0.156 (2)	0.0	0.61 (3)
O1′	0.288 (3)	0.096 (2)	0.5	0.61 (3)
O2	0.032 (2)	0.261 (1)	0.283 (2)	0.61 (3)
O2′	(0.032	0.261	0.717)	0.61 (3)
O3	0.0	0.5	0.206 (2)	0.61 (3)
O3′	(0.0	0.5	0.794)	0.61 (3)
O4	0.0	0.0	0.248 (2)	0.61 (3)
O4′	(0.0	0.0	0.752)	0.61 (3)
Dimensions (Å)	5.8825 (5), 11.7822 (4), 8.2293 (4)			
R_{wp}	0.1013			
S	4.47			

converge either to the model refined in *Pbam* symmetry or some other structure with a lower value of R_{wp}. It is most likely that the refinement in *Pba*2 was ill-conditioned and converged to a false minimum owing to the large number of parameters involved. Exploring this further, when we took the optimum model in *Pbam* symmetry, manually randomized some of the parameters and refined them in *Pba*2 symmetry, the system always converged to a structure very close to the *Pbam* structure with essentially the same R_{wp} factor. Particularly because fewer parameters are associated with *Pbam* than with *Pba*2, we conclude that the symmetry of the AFE structure at $T = 20$ K is centrosymmetric *Pbam*, in agreement with FSAS. The structural parameters refined in *Pbam* symmetry are listed in Table 1.

While many of the refined atomic coordinates thus determined are also in reasonable agreement with the values obtained by FSAS, as in Table 1, notable differences were found between those of the O atoms. In the case of a rotation of a perfect octahedron, the displacements of all O atoms would have the same magnitude. Any difference in the magnitude of the displacements implies distortion of oxygen octahedron. Since the present refinement gives much smaller differences among the displacements of different O atoms, in our model the oxygen octahedra are less deformed than in the FSAS structure.

3.2. *High-temperature phases*

In order to investigate evolution of the structural parameters data were collected for the AFE phase at T = 20, 100, 150, 200, 300 and 473 K, and for the intermediate phase at T = 508 K. Results of the Rietveld refinements for the AFE phase are shown in Table 2. Although the refined structure with *Pbam* symmetry shows good agreement with the data for the AFE phase, the fit slowly becomes worse with increasing temperature. At the same time, most structural parameters evolve smoothly with temperature. The strongest temperature dependence was observed for the orthorhombic lattice constant c. On the other hand, the orthorhombic lattice constants a and b are only weakly dependent on temperature, as shown in Table 2. Since the distortion of the cubic perovskite unit cell is relatively small, for simplicity we will use the pseudocubic lattice constants for discussion hereafter. The orthorhombic lattice constants are related to the pseudocubic lattice constants a_p, b_p and c_p through $a = 2a_p\cos(\beta/2)$, $b = 4b_p\sin(\beta/2)$ and $c = 2c_p$, where the β angle is 90°. At $T = 20$ K c_p is smaller than a_p and b_p and it increases rapidly with temperature. Consequently, all the pseudocubic lattice constants converge at higher temperatures. One possible explanation for this behavior may be in terms of oxygen octahedral tilting. An important consequence of tilting is to reduce the lattice constants in the directions perpendicular to the tilt axis (Glazer, 1975). Consequently, if the tilts about [100] and $[0\bar{1}0]$ are equal in magnitude, then a_p must be equal to b_p and larger than c_p. Also, combined tilts about [100] and $[0\bar{1}0]$ produce a $[1\bar{1}0]$ tilt which is present in the AFE phase of PZ. Therefore, an increase in the value of c_p may simply mean that the angle of the $[1\bar{1}0]$ tilt is

Table 2. *Rietveld-refined structural parameters for Pbam symmetry from the data collected at different temperatures*

The goodness-of-fit (S) agreement index is defined as R_{wp}/R_e, where R_e is the expected value of the R factor for perfect fitting.

	x	y	z	B
100 K				
Pb	0.703 (3)	0.123 (3)	0.0	0.44 (4)
Pb′	0.703 (3)	0.128	0.5	0.44 (4)
Zr	0.240 (3)	0.125 (2)	0.25	0.05 (2)
Zr′	(0.240	0.125	0.75)	0.05 (2)
O1	0.275 (3)	0.152 (2)	0.0	0.14 (3)
O1′	0.298 (3)	0.089 (2)	0.5	0.14 (3)
O2	0.032	0.262 (3)	0.278 (3)	0.45 (3)
O2′	(0.032	0.262	0.722)	0.45 (3)
O3	0.0	0.5	0.201 (2)	0.41 (3)
O3′	(0.0	0.5	0.799)	0.41 (3)
O4	0.0	0.0	0.229 (3)	0.40 (3)
O4′	(0.0	0.0	0.771)	0.40 (3)
Dimensions (Å)	5.8779 (4), 11.7846 (6), 8.2042 (6)			
R_{wp}	0.0799			
S	3.20			
150 K				
Pb	0.704 (2)	0.123 (2)	0.0	0.57 (3)
Pb′	0.704 (2)	0.128	0.5	0.57 (3)
Zr	0.240 (2)	0.125 (1)	0.25	0.09 (2)
Zr′	(0.240	0.125	0.75)	0.05 (2)
O1	0.275 (3)	0.152 (2)	0.0	0.14 (3)
O1′	0.298 (3)	0.089 (2)	0.5	0.14 (3)
O2	0.031	0.262 (2)	0.277 (3)	0.52 (3)
O2′	(0.031	0.262	0.722)	0.52 (3)
O3	0.0	0.5	0.200 (2)	0.42 (3)
O3′	(0.0	0.5	0.800)	0.42 (3)
O4	0.0	0.0	0.228 (3)	0.49 (2)
O4′	(0.0	0.0	0.772)	0.49 (2)
Dimensions (Å)	5.8775 (3), 11.7835 (4), 8.2088 (4)			
R_{wp}	0.0704			
S	3.13			
200 K				
Pb	0.705 (3)	0.124 (2)	0.0	0.77 (3)
Pb′	0.705 (3)	0.128	0.5	0.77 (3)
Zr	0.240 (2)	0.126 (1)	0.25	0.13 (2)
Zr′	(0.240	0.126	0.75)	0.13 (2)
O1	0.274 (2)	0.149 (1)	0.0	0.22 (2)
O1′	0.296 (2)	0.088 (1)	0.5	0.22 (2)
O2	0.031	0.262 (2)	0.276 (3)	0.59 (3)
O2′	(0.031	0.262	0.724)	0.59 (3)
O3	0.0	0.5	0.201 (2)	0.52 (3)
O3′	(0.0	0.5	0.799)	0.52 (3)
O4	0.0	0.0	0.229 (3)	0.68 (3)
O4′	(0.0	0.0	0.771)	0.68 (3)
Dimensions (Å)	5.8797 (3), 11.7827 (4), 8.2162 (3)			
R_{wp}	0.0701			
S	3.13			

Table 2 (*cont.*)

	x	y	z	B
473 K				
Pb	0.716 (3)	0.125 (2)	0.0	2.27 (3)
Pb′	0.716 (3)	0.126	0.5	2.27 (3)
Zr	0.242 (2)	0.127 (2)	0.25	0.22 (2)
Zr′	(0.242	0.127	0.75)	0.22 (2)
O1	0.270 (2)	0.142 (2)	0.0	0.72 (3)
O1′	0.288 (2)	0.087 (2)	0.5	0.72 (3)
O2	0.028	0.261 (2)	0.270 (3)	1.18 (5)
O2′	(0.028	0.261	0.730)	1.18 (5)
O3	0.0	0.5	0.206 (2)	1.00 (4)
O3′	(0.0	0.5	0.794)	1.00 (4)
O4	0.0	0.0	0.233 (3)	1.25 (4)
O4′	(0.0	0.0	0.767)	1.25 (4)
Dimensions (Å)	5.8808 (5), 11.7703 (6), 8.2539 (5)			
R_{wp}	0.0712			
S	3.48			

decreasing with increasing temperature. However, a decrease in the tilt angle would also be reflected in smaller displacements of the oxygen octahedra from the high-symmetry positions, which was not observed. On the contrary, oxygen displacements, with the only exception being the c displacement of O2, did not show any significant decrease. Therefore, it is not likely that the $[1\bar{1}0]$ tilt angle decreases with temperature and another cause for the increase in the orthorhombic lattice constant c must be located.

The value for the displacement factor on the Pb site was also seen to be anomalously large even at $T = 20$ K, as shown in Table 1. The reason is probably the presence of some static or quasistatic displacive disorder on the Pb site leading to a large uncertainty in the atom position. The previous structural determinations suggested the possibility of a Pb displacement in the c direction (JSMP; Dai *et al.*, 1995), but failed to characterize it. Our results showed that the large thermal factor for Pb increased more rapidly above $T = 200$ K than below. Since the behavior of the pseudocubic lattice constant c_p is similar to that of the Pb thermal factor, we speculate that the Pb displacement in the c direction becomes either more ordered or larger around 200 K and produces an increase in the pseudocubic lattice constant c_p.

In order to characterize the Pb displacement in the c direction we evaluated the effect of Pb displacements on the weighted Rietveld reliability factor R_{wp}. Since the mirror symmetry perpendicular to the c direction in *Pbam* prohibits the c displacement of Pb, refinement had to be carried out in non-centrosymmetric *Pba*2, keeping the balanced oxygen positions unchanged. The best-fit R_{wp} factor as a function of the static displacement of Pb in the c direction is shown in Fig. 2. We observed a flat minimum which becomes increasingly broad up to 300 K. The fact that the best-fit R_{wp} factor curves do not diverge immediately upon introducing a displacement of Pb along **c** indicates that the presence of static or quasistatic local Pb displacements is probable. Thus, from Fig. 2 it is conjectured that the local Pb displacements above and below the plane can take place with magnitudes up to 0.08 ± 0.02 Å at 100 K and 0.12 ± 0.02 Å at 200 K. At 473 K the curve fell to a shallow minimum at $\Delta = 0.08$ Å before finally diverging at larger values of Δ. For comparison, the best-fit R_{wp} factor diverged very quickly ($\Delta < 0.013$ Å) for the a axis Pb

distortion, as in the cases of all other Pb displacements except in the *c* direction. This indicates that all other Pb displacements cannot be reconciled with the data and should be rejected. The minimum in the R_{wp} factor with the Pb *c* displacement, however, is so shallow that it is not clear if it really indicates the development of an FE phase. That no FE transition has been reported between room temperature and 473 K suggests that the *c* displacements of Pb are probably local and disordered. Further evidence is the anomalously large values of the thermal factors for the Pb atoms. Our conjecture is that the *c*-axis Pb displacements are basically random, but may be locally pinned by some lattice defects to produce a very small spontaneous polarization. This observation is in agreement with recent measurements that showed a very small spontaneous polarization along the *c* direction in PZ (Dai *et al.*, 1995).

The Rietveld analysis for the intermediate phase did not proceed quite as smoothly as for the low-temperature phase. Refinement in both *Pba*2 and *Pbam* symmetries gave poor fits with large thermal factors on all atomic sites. For example, the Pb thermal factor increased more than twofold between 473 and 508 K. At the same time, other refined parameters changed significantly. Most notably, the refinement in *Pba*2 symmetry shows strong dependence on the Pb *c* displacement with a clear minimum at 0.13 Å. It also is important to note that axial-oxygen displacements differ in these models, even in direction. This behavior can be explained as originating from either an inadequate choice of symmetry or the existence of disorder in the axial-oxygen positions. Indeed, agreement was the best (R_{wp} = 0.0846) with the axial-oxygen disorder model. Thermal factors for all O atoms, with the exception of axial O3, were refined to significantly lower values as well, as shown in Table 2. Large thermal factors were still present only at the Pb sites. This is not a surprise since axial O atoms and Pb atoms are in-plane and a change in axial-oxygen displacements would have effects on the Pb atoms. Therefore, we suspect that the pattern of Pb displacements in the *ab* plane changed with increasing temperature and is not described correctly by either the *Pbam* or *Pba*2 symmetries.

It is also important to note that the diffraction pattern of the intermediate phase includes well defined superlattice peaks which can be indexed as $\frac{1}{2}\{110\}$ reflections, as shown in Fig. 3. They have been previously observed for the intermediate phase by neutron diffraction (Fujishita & Hoshino, 1984) and TEM (Viehland, 1995). Viehland (1995) attributed these reflections to a soft M_3 oxygen rotational mode. On the other hand, Fujishita & Hoshino (1984) proposed that this superlattice ordering was due to antiparallel displacements of cations and O atoms. We will address the question of the nature of this superlattice ordering in §4.

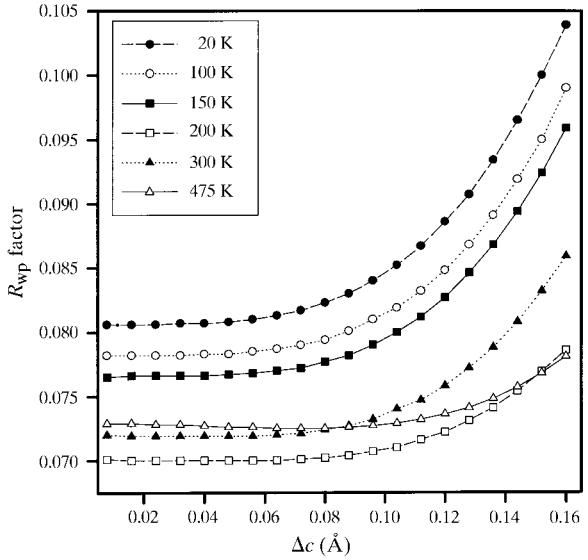

Fig. 2. Plots of the best-fit weighted profile R_{wp} factor *versus* static displacement of Pb in the *c* direction at different temperatures. Values were refined in *Pba*2 symmetry.

4. Pair distribution function refinements

4.1. *Experimental*

The Rietveld crystallographic analysis involves least-squares fitting of a diffraction pattern calculated from a model crystal structure to a measured diffraction pattern in momentum (Q) space. This type of analysis considers only the Bragg diffraction from a translationally invariant crystal and provides lattice constants and unit-cell atomic positions that describe long-range order in the structure. However, if the assumption of perfect periodicity is not satisfied and the local and global structures differ, this technique does not provide a complete picture of the atomic structure. By using only the Bragg

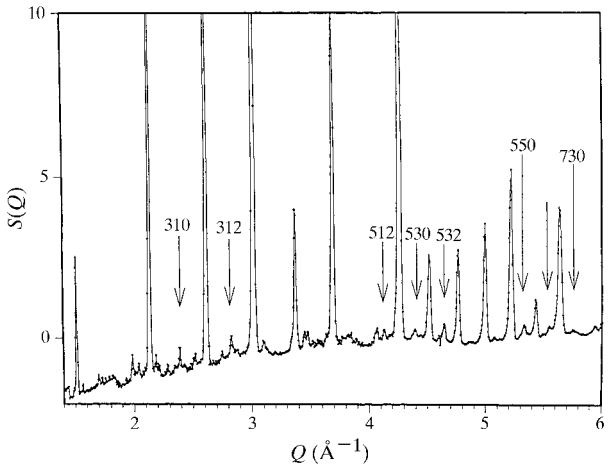

Fig. 3. Total structure factor $S(Q)$ for PZ in the intermediate phase obtained from the neutron powder diffraction data taken at T = 508 K. The $\frac{1}{2}\{110\}$ superlattice peaks, $\frac{1}{2}\{hkl\}$, are labeled *hkl*.

diffraction and ignoring the diffuse scattering, information on local deviations from the average structure is not sufficiently retained. Differences between the short-range structure and the long-range structure can only be approximated with large thermal vibrational amplitudes or an artificial disorder model with partial occupation of atomic sites. These difficulties may be overcome through the use of the pair distribution function (PDF) analysis.

The PDF, $\rho_o g(r)$, represents the distribution of interatomic distances and can be obtained through Fourier transformation of the scattering intensity normalized and corrected for background, absorption, multiple scattering and detector efficiency (Toby & Egami, 1992) according to

$$\rho_0 g(r) = \rho_0 + [1/(2\pi^2 r_0)] \int_0^\infty Q[S(Q) - 1] \sin(Qr) \mathrm{d}Q, \tag{1}$$

where ρ_o is the mean density, $S(Q)$ is the total structure function and $Q = |\mathbf{Q}| = 4\pi \sin\theta/\lambda$, where $\mathbf{Q}$ is the scattering vector. This expression yields the atomic density–density correlation in real-space units. At distances smaller than the atomic separation $\rho_0 g(r)$ is zero, while at large distances $\rho_o g(r)$ converges to ρ_0. The upper limit of integration in (1) is limited by the wavelength of the probe. Since $S(Q)$ approaches unity at large Q, owing to the Debye–Waller factor, as long as the cut-off value of Q is large enough the PDF can be calculated accurately. This can be achieved by collecting the data up to 30–40 Å^{-1} in Q (d = 0.15–0.2 Å) (Toby & Egami, 1992). This requires 0.3–0.4 Å in terms of the wavelength of the scattering probe to obtain $S(Q)$. Neutrons with such short wavelengths are abundantly available from a pulsed neutron source, which provides a large flux of high-energy epithermal neutrons.

In our experiments neutron powder diffraction data are collected using a time-of-flight spectrometer with no energy discrimination at the detector. Since both static and dynamic effects contribute to the scattering intensities, it is usually not possible to distinguish whether observed disorder is static or dynamic in nature, except when the energy scale of the dynamics is comparable to that of the neutron dynamics (McQueeney & Egami, 1998). Measurements are also made to determine the instrumental background, including scattering from the sample environment chamber. In the case of low-temperature measurements the sample environment is a Displex helium refrigerator mounted with all the heat shields in place and for high-temperature measurements it is a furnace. A separate experiment is carried out to measure the scattering from the empty sample container mounted with the full sample environment in place. Finally, in order to characterize the source spectrum and the detector efficiency, data are collected from a reference sample. For this purpose a solid rod of vanadium is used, with no special environment.

4.2. *Refinements*

The PDF of a model structure can be calculated by counting all interatomic distances. The PDF thus obtained is composed of a large number of δ functions corresponding to each interatomic distance in the model. However, in reality atoms are not static owing to quantum and thermal oscillations. These effects are simulated by convoluting the δ functions with normalized Gaussian functions. The standard deviation of the Gaussian, for a distance between two atoms, is calculated as the sum of their mean-square displacements.

A good structural model can be built by minimizing the so-called agreement factor (A factor), which is a measure of deviations in the PDF over an interval (r_a, r_b), defined by

$$A^2 = \left\{ \int_{r_a}^{r_b} [g_{\mathrm{obs}}(r) - g_m(r)]^2 \mathrm{d}r \right\} \Big/ \int_{r_a}^{r_b} \mathrm{d}r, \tag{2}$$

where $\rho_o g_{\mathrm{obs}}(r)$ and $\rho_o g_m(r)$ are experimental and model PDF's, respectively. Since every point in the PDF depends upon every point in $S(Q)$ *via* the Fourier transform, the statistical error at each point in the experimental PDF, $\sigma_{\mathrm{PDF}}(r)$, can be estimated by direct propagation of the s.u. of the diffraction data (Toby & Egami, 1992). Thus, the expected A factor when the model exactly describes the structure of the sample, or the minimum A factor (A_{min}), can be calculated by integrating $[\sigma_{\mathrm{PDF}}(r)]^2$ over the same range (Toby & Egami, 1992). This yields a good estimate of χ^2, given by

$$\chi^2 = A^2/A^2_{\mathrm{min}} \tag{3}$$

(Billinge, 1992). We used the square root of this value, S, to describe the goodness-of-fit.

In this work the PDF was examined to find evidence of significant displacements of atoms from their average crystallographic positions. Initially, the PDF's calculated from the Rietveld-refined models at different temperatures were compared with the data PDF's. Then, real-space refinements were carried out at each temperature. The modeling process consists of identifying possible atom displacements, even if they break the *Pbam* symmetry, and refining their values by minimizing the A factor. At the same time, the number of parameters must be kept to a minimum in order for the results of the modeling to be meaningful (Egami, 1995). In the PDF analysis at lower temperatures we refined just 28 parameters including positional and thermal parameters and the $S(Q)$ normalization factor. For comparison, in the crystallographic refinement we refined 27 structural parameters in *Pbam* symmetry and 30 in *Pba*2, in addition to 9 parameters which include the scale factor, background, extinction and absorption parameters. At higher temperatures the number of independent structural parameters in the PDF refinement is slightly larger, 34, owing to oxygen disorder. The A factor was minimized using the Monte Carlo simulated annealing

Table 3. *Structural parameters refined by the pair distribution function analysis of the data collected at different temperatures*

The goodness-of-fit (S) agreement index is defined as A/A_e, where A_e is the expected value of the A factor for perfect fitting.

	x	y	z	B		x	y	z	B
20 K					200 K				
Pb	0.704 (2)	0.125 (2)	0.000 (2)	0.10 (1)	Pb	0.704 (2)	0.123 (2)	0.007 (2)	0.24 (1)
Pb′	0.704 (2)	0.125 (2)	0.500 (2)	0.10 (1)	Pb′	0.704 (2)	0.127 (2)	0.507 (2)	0.24 (1)
Zr	0.245 (2)	0.125 (2)	0.250 (2)	0.07 (1)	Zr	0.240 (2)	0.125 (2)	0.250 (2)	0.15 (1)
Zr′	0.245 (2)	0.125 (2)	0.750 (2)	0.07 (1)	Zr′	0.240 (2)	0.125 (2)	0.750 (2)	0.15 (1)
O1	0.279 (2)	0.153 (2)	0.000 (2)	0.12 (1)	O1	0.279 (2)	0.150 (2)	0.000 (2)	0.17 (1)
O1′	0.303 (2)	0.091 (2)	0.500 (2)	0.12 (1)	O1′	0.307 (2)	0.096 (2)	0.500 (2)	0.17 (1)
O2	0.034 (2)	0.262 (2)	0.284 (2)	0.12 (1)	O2	0.036 (2)	0.260 (2)	0.284 (2)	0.17 (1)
O2′	0.034 (2)	0.262 (2)	0.716 (2)	0.12 (1)	O2′	0.036 (2)	0.260 (2)	0.716 (2)	0.17 (1)
O3	0.000 (2)	0.500 (2)	0.201 (2)	0.12 (1)	O3	0.000 (2)	0.500 (2)	0.203 (2)	0.17 (1)
O3′	0.000 (2)	0.500 (2)	0.799 (2)	0.12 (1)	O3′	0.000 (2)	0.500 (2)	0.797 (2)	0.17 (1)
O4	0.000 (2)	0.000 (2)	0.229 (2)	0.12 (1)	O4	0.000 (2)	0.000 (2)	0.230 (2)	0.17 (1)
O4′	0.000 (2)	0.000 (2)	0.771 (2)	0.12 (1)	O4′	0.000 (2)	0.000 (2)	0.770 (2)	0.17 (1)
A (%)	8.11				A (%)	7.10			
S	3.77				S	3.54			
100 K					300 K				
Pb	0.704 (2)	0.125 (2)	0.005 (2)	0.14 (1)	Pb	0.704 (2)	0.126 (2)	0.007 (2)	0.32 (1)
Pb′	0.704 (2)	0.125 (2)	0.505 (2)	0.14 (1)	Pb′	0.704 (2)	0.126 (2)	0.507 (2)	0.32 (1)
Zr	0.245 (2)	0.125 (2)	0.250 (2)	0.11 (1)	Zr	0.240 (2)	0.125 (2)	0.251 (2)	0.19 (1)
Zr′	0.245 (2)	0.125 (2)	0.750 (2)	0.11 (1)	Zr′	0.240 (2)	0.125 (2)	0.751 (2)	0.19 (1)
O1	0.270 (2)	0.154 (2)	0.000 (2)	0.14 (1)	O1	0.279 (2)	0.149 (1)	0.000 (2)	0.21 (1)
O1′	0.305 (2)	0.093 (2)	0.500 (2)	0.14 (1)	O1′	0.306 (2)	0.097 (1)	0.500 (2)	0.21 (1)
O2	0.034 (2)	0.262 (2)	0.284 (2)	0.14 (1)	O2	0.032 (2)	0.261 (2)	0.284 (2)	0.21 (1)
O2′	0.034 (2)	0.262 (2)	0.716 (2)	0.14 (1)	O2′	0.032 (2)	0.261 (2)	0.716 (2)	0.21 (1)
O3	0.000 (2)	0.500 (2)	0.201 (2)	0.14 (1)	O3	0.000 (2)	0.500 (2)	0.208 (2)	0.21 (1)
O3′	0.000 (2)	0.500 (2)	0.799 (2)	0.14 (1)	O3′	0.000 (2)	0.500 (2)	0.792 (2)	0.21 (1)
O4	0.000 (2)	0.000 (2)	0.229 (2)	0.14 (1)	O4	0.000 (2)	0.000 (2)	0.231 (2)	0.21 (1)
O4′	0.000 (2)	0.000 (2)	0.771 (2)	0.14 (1)	O4′	0.000 (2)	0.000 (2)	0.769 (2)	0.21 (1)
A (%)	7.18				A (%)	7.47			
S	3.50				S	3.64			
150 K					473 K				
Pb	0.704 (2)	0.123 (2)	0.007 (2)	0.19 (1)	Pb	0.707 (2)	0.126 (2)	0.016 (2)	0.38 (1)
Pb′	0.704 (2)	0.127 (2)	0.507 (2)	0.19 (1)	Pb′	0.707 (2)	0.126 (2)	0.516 (2)	0.38 (1)
Zr	0.240 (2)	0.125 (2)	0.250 (2)	0.13 (1)	Zr	0.240 (2)	0.125 (2)	0.253 (2)	0.22 (1)
Zr′	0.240 (2)	0.125 (2)	0.750 (2)	0.13 (1)	Zr′	0.240 (2)	0.125 (2)	0.753 (2)	0.22 (1)
O1	0.278 (2)	0.151 (2)	0.000 (2)	0.15 (1)	O1	0.278 (2)	0.147 (2)	0.000 (2)	0.25 (1)
O1′	0.308 (2)	0.094 (2)	0.500 (2)	0.15 (1)	O1′	0.305 (2)	0.099 (2)	0.500 (2)	0.25 (1)
O2	0.034 (2)	0.262 (2)	0.284 (2)	0.15 (1)	O2	0.032 (2)	0.261 (2)	0.283 (2)	0.25 (1)
O2′	0.034 (2)	0.262 (2)	0.716 (2)	0.15 (1)	O2′	0.032 (2)	0.261 (2)	0.716 (2)	0.25 (1)
O3	0.000 (2)	0.500 (2)	0.202 (2)	0.15 (1)	O3	0.000 (2)	0.500 (2)	0.216 (2)	0.25 (1)
O3′	0.000 (2)	0.500 (2)	0.798 (2)	0.15 (1)	O3′	0.000 (2)	0.500 (2)	0.784 (2)	0.25 (1)
O4	0.000 (2)	0.000 (2)	0.229 (2)	0.15 (1)	O4	0.000 (2)	0.000 (2)	0.231 (2)	0.25 (1)
O4′	0.000 (2)	0.000 (2)	0.771 (2)	0.15 (1)	O4′	0.000 (2)	0.000 (2)	0.769 (2)	0.25 (1)
A (%)	7.26				A (%)	8.50			
S	3.56				S	3.95			

procedure (Toby & Egami, 1992) and refinements were carried out over the range $1.8 \leq r \leq 9.5$ Å. The maximum allowed number of independent parameters in this interval is 80 (Billinge, 1992), more than twice as many as we refined.

The PDF's for PZ at temperatures of $T = 20$, 300 and 473 K are shown in Fig. 4. As an example let us take values from the refinements of PZ at 20 K. The best-fit model, described in the next section, gave an A factor of 7.87% with $\sigma(A) = 0.12\%$ over the range $1.8 \leq r \leq 9.5$ Å. Over this range, $A_{\min}$ was 2.15% and, therefore, the value of S is 3.66. This value is comparable to the S value of 3.20 attained in the Rietveld refinement model of PZ at 20 K.

4.3. *Structure determination*

4.3.1. *Comparison with the Rietveld refinement results*. The results from the PDF refinement at different temperatures for the AFE phase are shown in Table 3. It is reassuring that the positions of most O atoms obtained from the Rietveld and PDF analyses are in very good

agreement at all temperatures, with differences between the two methods smaller than ±0.02 Å. However, the axial oxygen O1 and the equatorial oxygen O2 coordinates have refined to different values in the Rietveld and PDF analyses at all temperatures. For example, at 20 K the differences are 0.04 and 0.05 Å for the axial oxygen O1′(x) and equatorial oxygen O2(c), respectively. It is important to notice that the Rietveld-refined thermal factor is largest (B = 0.44 Å^2) for the equatorial oxygen O2(c) for which the difference in the refined values of displacement between the Rietveld and PDF analyses is largest. This value of B corresponds to an unreasonably high mean-square displacement, $\langle u^2 \rangle$, of 5×10^{-3} Å^2 compared with the PDF-refined value of 1.5×10^{-3} Å^2. If we use the frequency of the Zr—O stretch mode (Perry *et al.*, 1965) to estimate the Einstein temperature (Θ_E = 731 K), the value of $\langle u^2 \rangle$ calculated by the Einstein model is 2.07×10^{-3} Å^2 for O. Therefore, it is clear that the PDF analysis yields a much more reasonable estimate of the quantum and thermal oscillations of an O atom at T = 20 K, while the Rietveld refinement overestimates them.

In order to compare the refined variables in the Rietveld and PDF analyses it is important to estimate their accuracy. This is possible by considering the uncertainties in the A and R_{wp} factors and their best-fit curves as functions of a refined parameter, as illustrated in Fig. 5 for the equatorial-oxygen displacements in the c direction at 20 K. Since the s.u. for the A factor calculated by the propagation of the s.u. of the data (Toby & Egami, 1992) is ±0.12%, the uncertainties in O2(c), O3(c) and O4(c) parameters in the PDF analysis are ±0.01, ±0.02 and ±0.02 Å, respectively. Similarly, the s.u. of the R_{wp} factor is ±0.08%, so the uncertainties for O2(c), O3(c) and O4(c) are ±0.07, ±0.02 and ±0.04 Å, respectively, in the Rietveld analysis. Thus, the uncertainties in these positional parameters in the PDF analysis are significantly smaller than those in the Rietveld analysis. This trend in the sensitivities was found at all temperatures.

As an example, we compared the O2(c) coordinates refined by the Rietveld and PDF techniques. The difference between the two analyses for O2(c) are 0.06 Å at 200 and 300 K, and 0.10 Å at 473 K. The Rietveld-refined values for the thermal factor for O2 are 0.59, 0.80 and 1.18 Å^2 at these temperatures. They correspond to vibrational amplitudes of 0.09, 0.10 and 0.12 Å, respectively. On the other hand, the PDF-refined thermal factors for O2(c) are 0.14, 0.17 and 0.25 Å^2, which correspond to vibrational amplitudes of 0.04, 0.05 and 0.06 Å, at 200, 300 and 473 K, respectively. The latter values are more realistic as the phonon amplitudes. Taking into account the uncertainties for these two parameters, we see that the positions of O2 equatorial O atoms refined by the PDF analysis at temperatures above 100 K are inside the thermal spheres determined by the Rietveld analysis. The same holds for the positions of all other atoms at all temperatures. Therefore, we can conclude that the real-space refinement shows a greater sensitivity in distinguishing real thermal vibrations from small static or quasistatic atomic displacements away from the average crystallographic position. Consequently, the atomic positions refined by the PDF analysis are most likely to be more accurate.

4.3.2. *Low-temperature phase*. The PDF analysis of the 20 K data confirmed that displacements in the pseudocubic x and y directions follow the [1$\bar{1}$0] pattern. The thermal parameter for Pb obtained in the PDF analysis, B = 0.10 Å^2, is realistic and much smaller than the Rietveld-refined value of 0.25 Å^2. The best-fit model PDF is compared with the data PDF in Fig. 6. With increasing temperature the A factor becomes worse, but the local ferroelectric (FE) Pb displacement in the c direction improves the fit, as shown in Fig. 7. At temperatures of 100 and 150 K the curve for the best-fit A factor as a function of FE Pb$_c$ displacement shows shallow minima at ±0.04 and ±0.07 Å, respectively. At 200 K the minima shift to ±0.06 Å. The thermal factor at the Pb site, before introducing FE Pb displacements, increased to 0.14 and 0.19 Å^2 at temperatures of 100 and 150 K, respectively, which corresponds to a thermal displacement $\langle u^2 \rangle^{1/2}$ of approximately 0.05 Å. Thus, we can conclude that a small static or quasistatic local FE Pb displacement in the c direction developed. At a temperature of 200 K the thermal factor at the Pb site is 0.24 Å^2, corresponding to a thermal displacement of 0.06 Å.

Using the PDF analysis we can also detect the existence of correlation among Pb$_c$ displacements and its range. Keeping fixed the magnitude of the Pb$_c$ displacement that produced the best-fit model in the range 1.8–9.5 Å, we compared the PDF's with FE and random Pb$_c$ displacements for interatomic distances up to 40 Å. In the temperature range 100–200 K, the A factor is lower for the FE pattern at interatomic distances up to

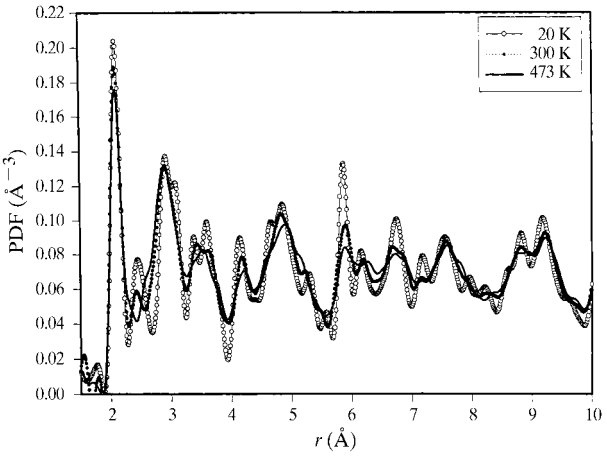

Fig. 4. Pair distribution functions for PZ at T = 20, 300 and 473 K.

10 Å. Beyond 10 Å, however, the random pattern shows better agreement with the data. Thus, we can estimate the FE correlation length at low temperatures to be about 10 Å, or approximately two pseudocubic unit-cell lengths. Therefore, the Pb displacements at low temperatures are only locally correlated and do not develop into bulk ferroelectric polarization. For this reason we conjecture that the Pb_c displacements must be quasistatic rather than static.

4.3.3. *High-temperature phases*. At 300 K the real-space refinement gave the best-fit model with an A factor somewhat larger than the best-fit A factors at lower temperatures. The refined in-plane Pb displacements were almost identical to the crystallographic AFE pattern. By contrast, the PDF refinement indicated FE Pb displacement in the c direction. Similar to the refinement at 200 K, the best-fit A-factor curve at 300 K showed two minima at $\Delta = \pm 0.06$ Å, with a width 0.11 Å at the 15% significance level, as shown in Fig. 7. The refined structural parameters and thermal factors changed little from low temperatures. However, some features of the experimental PDF are much more smeared at 300 K than at 20 K, Fig. 4. An increase in the thermal vibrational amplitude can account for only a

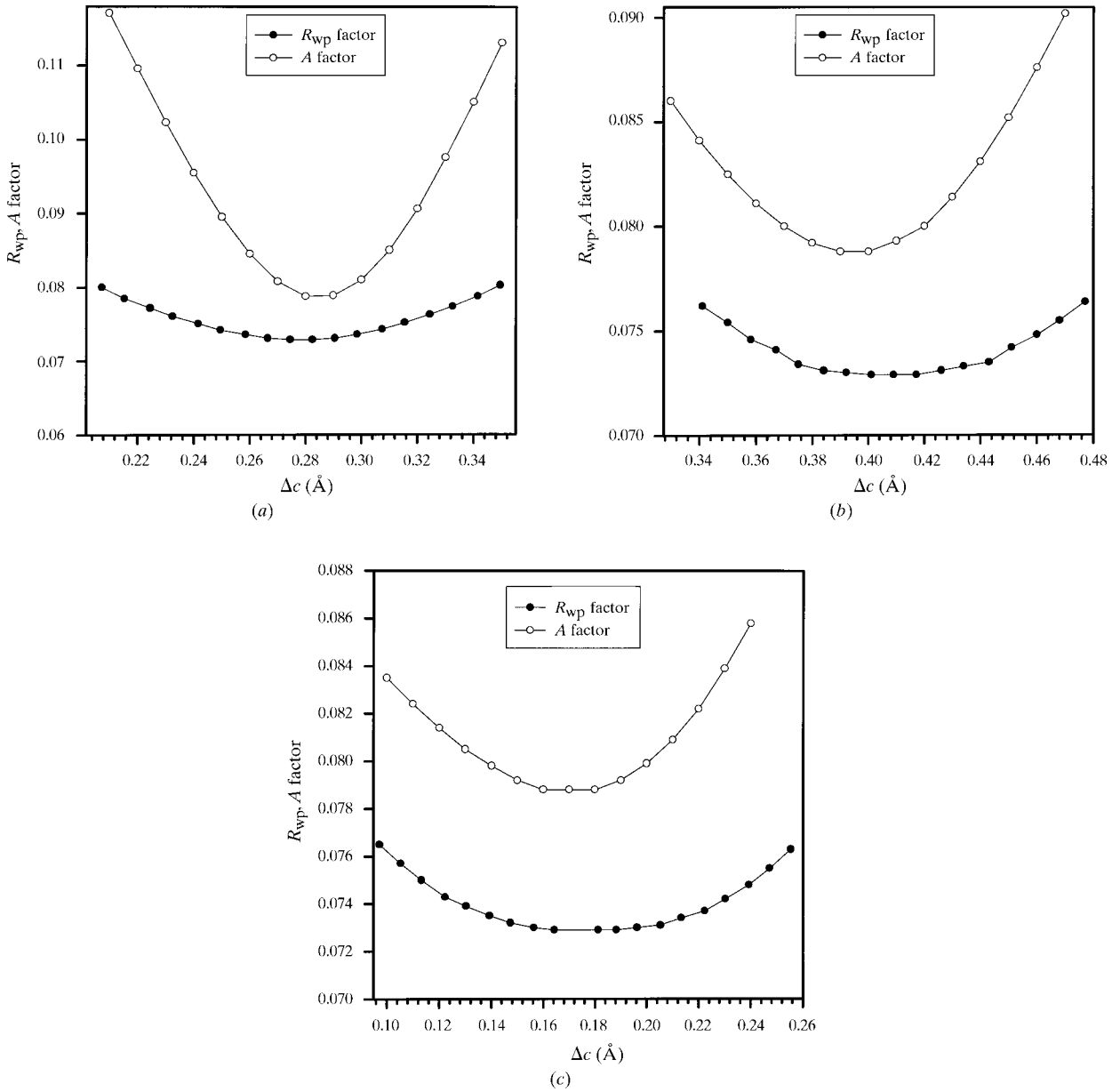

Fig. 5. The best-fit weighted profile R_{wp} factor, refined in *Pba2*, and the agreement A factor plotted against the displacement of the equatorial O atoms (*a*) O2, (*b*) O3 and (*c*) O4 by $\pm\Delta$ in the c direction for the data collected at $T = 20$ K.

small part of this change. For instance, the dramatic decrease in the height of the PDF peak at 5.9 Å, Fig. 4, cannot be explained by thermal phonons. This implies the existence of displacive disorder at room temperature. Displacive disorder associated with the Zr sublattice was not consistent with the data, in agreement with the small value of the thermal factors refined at the Zr site in the Rietveld analysis. Thus, displacive disorder at room temperature must exist on either the oxygen or Pb sites. Since, with the introduction of disorder, the number of possible structure models became immense, our goal in this modeling was to identify the essential features of the local structure rather than to establish a perfect model. Introducing disorder at the axial sites had no statistically significant effect in the Rietveld refinement. However, disordered oxygen displacements at the equatorial sites led to an improved fit. In *Pbam* symmetry equatorial sites are divided into two groups: O2 is in one group with O3 and O4 in the other. O3 and O4 are further differentiated since the Rietveld refinement showed different displacements in the *c* direction; at room temperature O3 is displaced by 0.41 Å and O4 by 0.17 Å. In the crystallographic structure, O3 and O4 are alternately displaced along [110]. Introducing disorder in the pattern of alternative O3 and O4 displacements improves the fit, lowering the *A* factor from 8.28 to 7.47%.

At 473 K both the reciprocal- and real-space refinements indicated an FE displacement of Pb in the *c* direction. The best-fit curve for the R_{wp} factor shows shallow minima at ±0.08 Å. In the PDF refinement the *A*-factor curve has somewhat deeper minima at ±0.14 Å before finally diverging at a larger value of Δ = 0.20 Å, as shown in Fig. 7. We investigated the range of the Pb correlations. In the range 10–20 Å the *A* factor for the FE Pb_c displacements is 3.73% compared with 3.92% for random Pb_c displacement. In this range $\sigma(A)$ = 0.10%. From 20 to 30 Å the *A* factor for the FE pattern of Pb_c displacements, 2.14%, is statistically equivalent to that for random displacements, 2.05%, since $\sigma(A)$ is 0.09%. In the range 30–40 Å $\sigma(A)$ is 0.08%, making random displacements with *A* = 2.51% better than the FE pattern with *A* = 2.64%. Therefore, we can conclude that the FE model shows the best fit with the data up to 20 Å and thus estimate the Pb_c correlation length to be ~ 20 Å.

Since features of the PDF at 473 K are even more smeared than at room temperature, where a degree of disorder at the oxygen positions was observed, we again tested the possibility of disorder in the oxygen positions in the PDF analysis. Equatorial-oxygen disorder lowered the value for the *A* factor from 9.39% for the ordered model to 8.87% and, therefore, the equatorial-oxygen disorder, first observed at 300 K, was also present at higher temperatures in the AFE phase. We also tested the possibility that the O atoms which are in-plane with Pb, namely the axial O1 and O1′, are disordered. In *Pbam* symmetry the direction of displacement of any axial oxygen was determined by the sense of [100] rotation of the oxygen octahedron to which it belongs and whether it was on the top (O1′) or bottom (O1) of the octahedron. At the same time, the magnitude was different for O1 and O1′, as may be seen by different relative displacements in the orthorhombic unit cell indicated in Table 3. The displacements of O1 and O1′ axial O atoms in the crystallographic axial-oxygen ordered model are shown in Fig. 8(*a*). Introducing displacive disorder in O1 and O1′ lowered the *A* factor somewhat, but did not statistically justify the introduction of a large number of parameters. Alternatively, one could also imagine disorder introduced by the random exchange of magnitudes of displacements between the

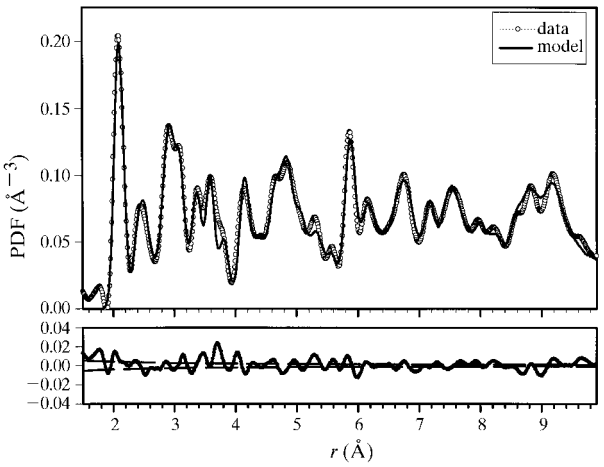

Fig. 6. The best-fit model PDF (solid line) superimposed on the data PDF (open circles) of PZ at *T* = 20 K. The difference plot in the expanded scale (observed minus calculated) is shown at the bottom together with dashed lines which indicate statistical errors of the data PDF.

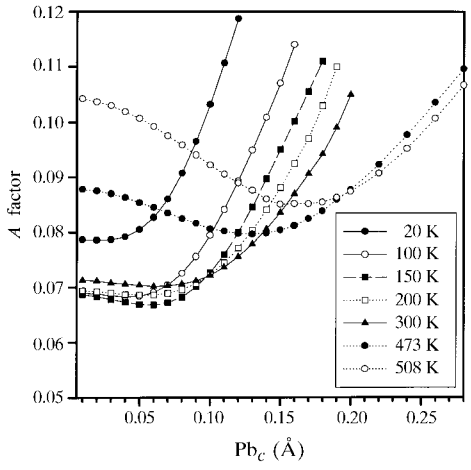

Fig. 7. Plots of the best-fit *A* factor as a function of FE Pb displacement in the *c* direction at different temperatures. Values were refined from the PDF.

top and bottom axial O atoms. An axial-oxygen disordered model consisting of $4 \times 4 \times 2$ cells is shown in Fig. 8(*b*). Introducing axial-oxygen disorder to the model with equatorial-oxygen disorder lowered the *A* factor to 8.50%. At room temperature the real-space refinement did not provide definite evidence in support of disorder in the axial O atoms, because it did not produce any change in the *A* factor. At higher temperatures, nevertheless, axial-oxygen disorder clearly improved the fit.

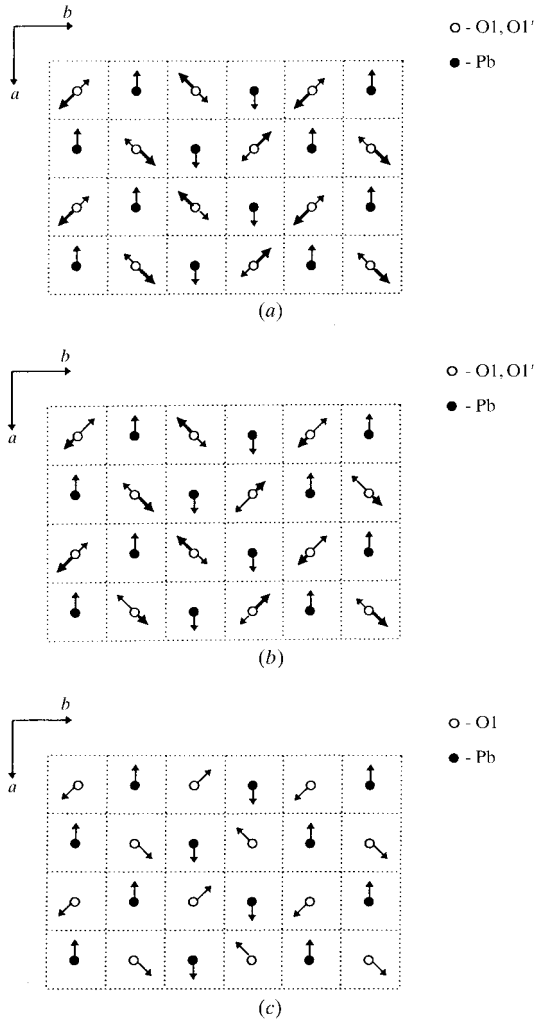

Fig. 8. The pattern of Pb- (solid circles) and oxygen-ion (open circles) displacements superimposed upon the network of oxygen octahedra: (*a*) low-temperature *Pbam* crystallographic structure, (*b*) axial-oxygen disordered structure and (*c*) axial-oxygen pattern observed in the intermediate phase. Open circles represent axial O atoms and equatorial O atoms (not shown) lie in the corners of the grid. Displacement of the top axial oxygen is shown with a bold arrow and that of the bottom axial oxygen with a regular arrow. The difference in magnitude between the displacements is exaggerated for the sake of clarity. In (*c*) only displacement of the top axial oxygen is shown for the sake of clarity. The corresponding bottom axial oxygen is displaced in the opposite direction. In the intermediate phase additional disorder in magnitudes of axial-oxygen displacement was refined.

Just as in the case of our Rietveld analysis discussed earlier, the PDF analysis of the intermediate phase did not proceed quite as smoothly as would normally be expected. Since at 473 K we had already observed disorder for both the axial and equatorial oxygen sites, we first introduced similar disorder in the model for the intermediate phase. Introducing disorder at both axial and equatorial sites improved the fit, from $A = 12.55$ to 10.62%, but it was still higher than at lower temperatures. Clearly, the model for the low-temperature AFE phase does not adequately describe the structure in the intermediate phase. This is in agreement with the conclusion of our Rietveld analysis that the displacement pattern of Pb and the axial oxygen at 508 K is qualitatively different from that at lower temperatures. To determine this pattern we used the low-temperature in-plane AFE pattern of Pb displacement and refined the directions of axial-oxygen displacements. The fit was significantly improved and led to an agreement factor of 9.10%. The refined axial-oxygen displacement pattern is compared with the crystallographic model in Fig. 9. We also refined FE Pb_c displacements to be 0.18 Å. When additional disorder in the magnitude of axial-oxygen displacement was introduced we obtained an *A* factor of 8.70%. The refined pattern of axial-oxygen and Pb displacements is shown in Fig. 9(*b*).

A different, simpler AFE pattern with alternating Pb displacements within the *ab* plane (AFE-II), as opposed to the double-row AFE pattern at low temperatures (AFE-I), provided the basis for good refinement of axial-oxygen displacements. While in the AFE-I pattern the high-temperature unit cell is quadrupled in the [110] direction, in the AFE-II pattern it is only doubled. The refined axial-oxygen and Pb pattern is shown in Fig. 10(*b*). In analogy to the best-fit model at 473 K, we introduced disorder in the magnitudes of the axial-oxygen displacements and obtained a slightly better fit, with $A = 8.54\%$. The refined value for Pb *c* displacement was 0.20 Å. It is important to notice that this pattern does not reflect either *Pbam* or *Pba*2 symmetry. On the other hand, the $\frac{1}{2}\{110\}$ superlattice peaks observed in the diffraction pattern, Fig. 3, can be explained with this AFE-II ordering in the *ab* plane.

The difference between the agreement factors for the two competing models with different AFE patterns of Pb displacements is very small and they both describe the local structure equally well. However, the presence of sharp, well defined superlattice diffraction peaks implies that the ordering in the AFE-II pattern is long range. Thus, two possibilities can be considered; one is that two phases with AFE-I and AFE-II ordering coexist and the other is that the long-range order is described by the AFE-II ordering, while locally AFE-I type structural fluctuations are abundantly observed. The first case would result in two overlapping diffraction patterns, most likely with slightly different lattice constants, thus broadening the diffraction peaks slightly. However, such

peak broadening was not observed. Thus, we believe that the second case describes the intermediate phase most correctly. In the case of the second-order phase transition it is not unusual to observe the structure of the low-temperature phase forming locally as fluctuations in the high-temperature phase, particularly near the phase transition temperature (Stern & Yacoby, 1996). Since the temperature range for the intermediate phase is so small, the temperature 508 K, at which the measurement was performed, is very close to the phase transition temperature (501 K). Consequently, many small domains of the low-temperature AFE-II structure must have been formed locally as a result of thermal fluctuations. Therefore, it is not surprising that our Rietveld refinement at 508 K in these symmetries was not very successful since significant structural disorder makes the Rietveld analysis more difficult and less reliable. In contrast, the real-space analysis is not affected by disorder since the PDF analysis does not presume periodicity. In fact, the PDF accurately describes the local structure even in the total absence of periodicity, as in glasses.

A large FE Pb displacement in the c direction was observed in the Rietveld analysis of the intermediate phase. The PDF-refined values of Pb_c are 0.18 for AFE-I and 0.20 Å for AFE-II. The FE pattern of Pb_c displacements describes best not only the short-range structure, but also the intermediate-range structure. We compared the PDF for the model of the structure with the low-temperature AFE pattern of Pb displacements with the experimental data for distances up to 40 Å. In the range 10–20 Å the A factor for the FE pattern of Pb_c displacement is 4.88%, compared with 5.01% for random Pb_c displacement. In this range $\sigma(A)$ is 0.10%. From 20 to 30 Å $\sigma(A)$ is 0.09% and the A factor for the FE pattern of Pb_c displacement, 3.14%, is signifi-

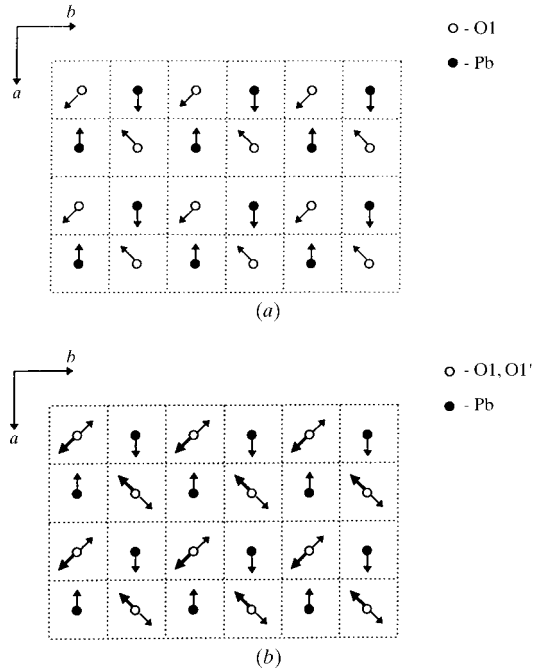

Fig. 9. The AFE-II pattern of Pb- (solid circles) and oxygen-ion (open circles) displacements superimposed upon the network of oxygen octahedra: (*a*) only displacement of the top axial oxygen is shown for the sake of clarity; (*b*) displacements of both the top (bold arrow) and bottom (regular arrow) axial O atoms are shown. Open circles represent axial O atoms and equatorial O atoms (not shown) lie in the corners of the grid. In the intermediate phase additional disorder in magnitudes of axial-oxygen displacement was refined. The low-temperature *Pbam* crystallographic structure (AFE-I pattern of Pb displacements) is shown in Fig. 8(*a*).

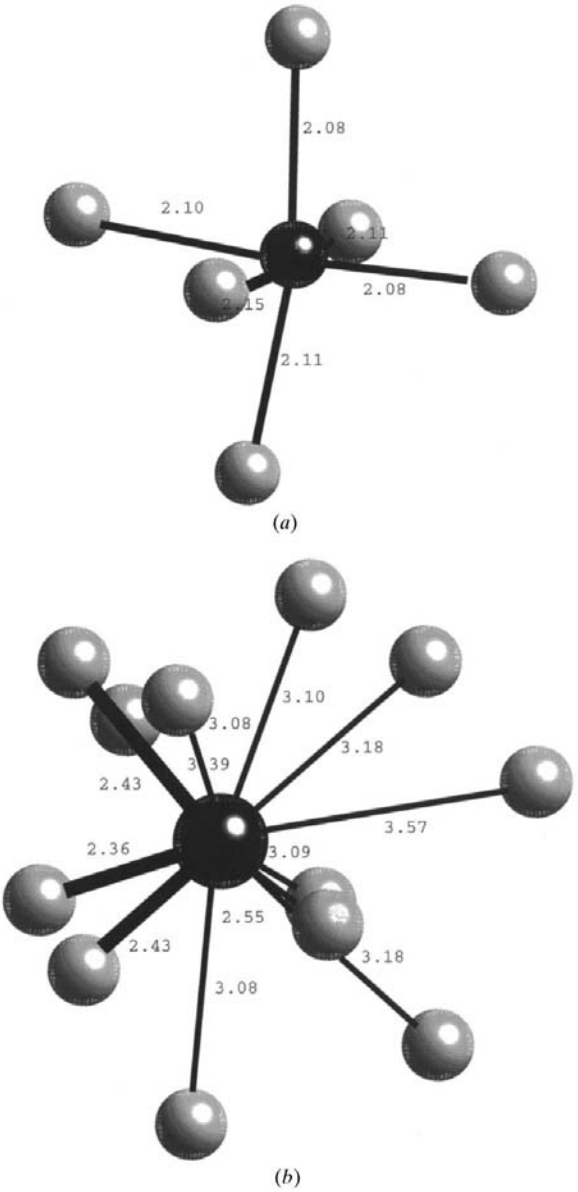

Fig. 10. (*a*) The ZrO_6 octahedron obtained by the present study. (*b*) The Pb environment. Three closest Pb and O atoms are connected with bold lines. Interatomic distances are given in Å.

Table 4. *Pb—O bond lengths (Å) refined by the pair distribution function analysis at different temperatures*

Fujishita *et al.* (1982)	20 K	100 K	150 K	200 K	300 K	473 K
2.35	2.37	2.37	2.37	2.38	2.37	2.37
2.46	2.42	2.42	2.42	2.38	2.39	2.39, 2.55
2.47	2.42	2.42	2.42	2.47	2.48	2.57
2.47	2.58	2.56	2.56	2.62	2.62	2.62
2.81, 3.06	2.92, 3.09	2.90, 3.08	2.90, 3.08	3.00	2.88, 2.99	2.79, 2.84
2.81, 3.06	2.92, 3.09	2.90, 3.08	2.90, 3.08	3.05	2.97, 3.05	2.92, 3.01
3.07	3.09	3.08	3.08	3.10	3.08	3.05
3.07	3.09	3.08	3.08	3.12	3.12	3.10
3.08, 3.31	3.19, 3.34	3.17, 3.35	3.17, 3.33	3.14	3.14, 3.24	3.30, 3.35
3.08, 3.31	3.19, 3.34	3.17, 3.35	3.17, 3.33	3.23	3.22, 3.32	3.30, 3.35
3.44	3.37	3.39	3.38	3.33	3.33	3.35

cantly smaller than for random displacement, 3.38%. In the range 30–40 Å $\sigma(A)$ is 0.08%, while the A factors for the FE and random displacements are 3.50 and 3.58%, respectively, making both statistically equivalent. Therefore, we can conclude that the local FE model for Pb_c displacement shows the best fit with the data up to 30 Å, while it is inconclusive whether the FE long-range order is established.

Although PZ at high temperatures (above 508 K) was crystallographically refined as cubic, very small differences were observed in the PDF between 508 and 523 K. This implies that the PE phase is locally polarized and that the FE phase transition is of the order/disorder type (Stern & Yacoby, 1996). The PDF refinement of the data at 523 K showed that Pb atoms were displaced along [111]. The displacements are not correlated from site to site and, therefore, are not directly observable in the reciprocal-space analysis, but only indirectly, through the anomalously large thermal factors refined in the Rietveld analysis.

5. Discussion

5.1. *Low-temperature phase*

One of the principal features of the present findings is that at all temperatures the c displacements of O atoms are balanced. Therefore, no spontaneous polarization is caused by O atoms, in disagreement with JSMP. It is important to note that the total electronic energy calculation by Singh (1995) also raised questions of reliability of the oxygen positions refined by JSMP and FSAS. The calculations revealed substantial forces on the axial and O4 equatorial O atoms in the model by FSAS. The refined oxygen positions obtained by this calculation are in excellent agreement with our model.

The dual-space refinement of the AFE phase shows that Pb atoms are displaced in the c direction, in addition to the antiparallel shifts within the ab plane. These displacements are observable at 100 K and increase in magnitude with temperature. They are spatially correlated and the range of correlation increases slowly with temperature: from just ~ 10 Å at room temperature to 30 Å or more in the intermediate phase. In PZ, therefore, the measured c-axis polarization (Dai *et al.*, 1995) is most probably due only to the Pb displacement in the c direction and this explains why it is small (Slater, 1950).

Owing to the lone-pair sp electrons, a Pb atom is highly deformable (Cohen, 1992) and can form stronger covalent bonding with a smaller number of oxygen neighbors. In an ideal perovskite Pb is surrounded by 12 O atoms at an equal distance, but tilting of the octahedra around the $[1\bar{1}0]$ axis changes the Pb environment. The lone-pair electrons of Pb form covalent bonds with the closest O atoms that are grouped together in certain directions, so that Pb becomes off-center from its high-symmetry position, causing further splittings in the Pb—O distances. This off-centering should result in a significant dipolar moment of the PbO_{12} cluster. Our PDF-refined values for the Pb—O distances are shown in Table 4 and compared with the values obtained by FSAS. In both models a Pb and the three closest O atoms (an axial and two equatorial O atoms) form a distorted PbO_3 tetrahedron, Fig. 10(b). We refined the distances between Pb and the O atoms at the corners of such a tetrahedron to be 2.37, 2.42 and 2.42 Å at 20 K and 2.37, 2.39 and 2.48 Å at 300 K. The direction of the normal from the plane of these three O atoms to the Pb atom is approximately in the $[1\bar{1}0]$ direction in the original cubic lattice. FSAS also refined a fourth short Pb—O distance (2.46 Å) in a direction almost perpendicular to the normal of the base of the triangle. In our PDF refinement this O atom is further removed from Pb by 0.11 Å than in the FSAS model, as shown in Table 4.

These short Pb—O distances are not new in the literature concerned with the structure of lead oxides. In the structure of orthorhombic or yellow PbO, Pb—O distances are 2.21, 2.22 and 2.49 Å and the Pb and three O atoms form a trigonal pyramid (Kay, 1961). In the tetragonal red PbO the Pb atom is close to a square of O atoms and the Pb—O distance is 2.317 Å (Leciejewicz, 1961). Also, in the FE phase of $PbTiO_3$ the equatorial O atoms form a flat tetragonal pyramid with Pb at the apex and a Pb—O distance of 2.52 Å at room temperature (Glazer & Mabud, 1978). The distance between Pb and the axial O atoms is 2.80 Å and further away are four other equatorial O atoms at a distance of 3.21 Å (Glazer & Mabud, 1978). In the structures of both orthorhombic

PbO and tetragonal $PbTiO_3$, PbO_4 pyramids share corners forming continuous two-dimensional sheets. In PZ, as discussed above, Pb atoms form PbO_3 tetrahedra with the spatial distribution and arrangement of these PbO_3 tetrahedra determining the long-range structure. In the low-temperature AFE-I structure the PbO_3 tetrahedra in alternating [001] layers have different arrangements: in one layer the tetrahedra group by sharing an edge and forming isolated Pb_2O_4 groups and in the other layer the tetrahedra are not connected. If all Pb displacements in PZ were aligned making an FE pattern in the *ab* plane, none of the PbO_3 tetrahedra would be connected. In contrast, the high-temperature AFE-II pattern of Pb displacements would produce equivalent [001] layers of edge-shared PbO_6 octahedra.

5.2. *High-temperature phases*

In the intermediate phase the PDF analysis indicated two structural models with distinct patterns of Pb displacements in the *ab* plane; one with double rows of opposite Pb displacements along the $[1\bar{1}0]$ direction, which is the low-temperature phase AFE-I pattern, and the other with alternating single rows, the AFE-II pattern. Different axial-oxygen displacements were also refined for each model. The structural disorder observed by the Rietveld analysis may be explained by the coexistence of these two types of atomic arrangements. The $\frac{1}{2}\{110\}$ superlattice peaks at 508 K reflect the long-range AFE-II Pb displacements in the intermediate phase. However, the proximity in temperature to the low-temperature phase must have resulted in local structural fluctuations in the low-temperature AFE-I ordering. Each Pb displacement pattern was accompanied by a distinct oxygen arrangement. Since the Pb and axial O atoms lie in the same plane, it is expected that they interact strongly and that displacements of one cause shifts in the other.

Previously Fujishita & Hoshino (1984) observed $\frac{1}{2}\{110\}$ peaks in the neutron diffraction spectrum and attributed them to antiparallel displacements of cations and O atoms. On the other hand, Viehland (1995) believed that the origins of the $\frac{1}{2}\{110\}$ reflections were due to an M_3 oxygen rotational mode. This mode involves the rotations of successive oxygen layers in the same direction. In contrast, the R_{25} mode, which is present in the low-temperature AFE phase, involves rotations of successive oxygen layers in opposite directions. Therefore, some of the second-nearest-neighbor O—O distances should increase in the case of the R_{25} mode. However, if the M_3 mode is present, there will be no change in the O—O second-neighbor distances. The experimental PDF's at 473 and 508 K are compared in Fig. 11. Since the O—O PDF peak at 508 K appears at a larger value of r than at 473 K, the explanation of the $\frac{1}{2}\{110\}$ superlattice peaks in terms of the M_3 mode is not consistent with the data.

While the AFE-II pattern of Pb displacements in the intermediate phase is a conventional antiferroelectric pattern consisting of alternating single [110] rows of Pb atoms, the pattern in the low-temperature AFE-I phase is composed of double rows of Pb displaced in an alternating fashion. In order to understand this unusual structure it is useful to consider the arrangements of PbO_3 tetrahedra. As we discussed above Pb polarization occurs by a Pb atom attracted to a triangle of O atoms, forming a covalently bonded PbO_3 tetrahedron. In both AFE-I and AFE-II patterns, two of these tetrahedra are grouped by sharing an edge. A Pb_2O_4 cluster is formed with the two Pb atoms displaced in opposite directions. In the low-temperature AFE-I structure two neighboring Pb_2O_4 clusters belonging to different double [110] rows of Pb are configured in a π-rotated pattern. Consequently, the two adjacent Pb atoms belonging to two different clusters are displaced in the same direction and in this way the dipolar moments of the two PbO_{12} clusters are kept away from each other, as shown in Fig. 12. In the intermediate AFE-II structure the two adjacent Pb atoms belonging to the two neighboring Pb_2O_4 clusters are displaced in opposite directions, so that the dipolar moments of the neighboring PbO_{12} clusters are opposing each other, increasing the Coulomb repulsion energy. This explains why the AFE-I pattern is preferred over the AFE-II pattern at low temperatures. In the intermediate phase, however, Pb atoms are additionally displaced along the c direction ($Pb_c = 0.20$ Å). Thus, the dipolar moments of the PbO_{12} clusters are tilted away from the *ab* plane. This tilting increases the distance between the two adjacent PbO_{12} clusters and decreases the energy of this configuration. At the same time, the entropy of the AFE-II pattern is higher because of the allowed choices in the directions of the c displacements of the Pb ions. It is possible and likely that this entropic

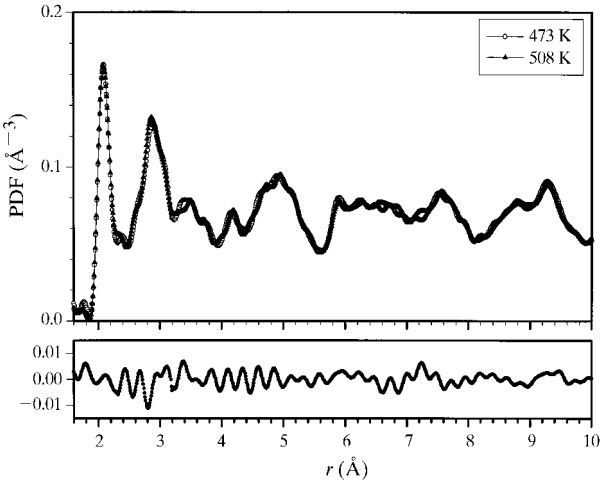

Fig. 11. Pair distribution functions for PZ at T = 473 and 508 K. The difference plot (PDF at 473 K minus PDF at 508 K) is shown at the bottom in the expanded scale.

effect stabilizes the AFE-II pattern at the intermediate temperatures.

It is interesting to note the similarity between the PDF-refined disordered pattern in axial-oxygen displacements in the intermediate phase and the pattern of O atoms in the model by Glazer *et al.* (1993). They refined the single-crystal structure of PZ at room temperature and found that the structure is disordered, having two identical substructure components related by a shear of $c/2$. In order for such a shear to take place, local oxygen vacancies to provide broken bonds are necessary. Although a shear disorder has not been seen in ceramic samples, it is interesting to compare this crystallographic shear structure with the PDF refinement results. First, the substructure symmetry is *Pbam* and the refined atomic positions are very similar to the values refined in this work. The only difference stems from the missing bonds in the model by Glazer *et al.* (1993), which would produce only a decrease in the Pb—O peak height in the PDF, but not changes in its position or shape. In the PDF-refined model equatorial O atoms are rotated around the same $[1\bar{1}0]$ axis, and no vacancies are needed to account for the disorder. However, shear on the oxygen octahedra owing to the disorder in the axial-oxygen displacements is somewhat larger than in the model by Glazer *et al.* (1993). It is quite possible that a difference in stoichiometry between the crystals and ceramics led to different internal strains, which caused displacive disorder of oxygen at different temperatures.

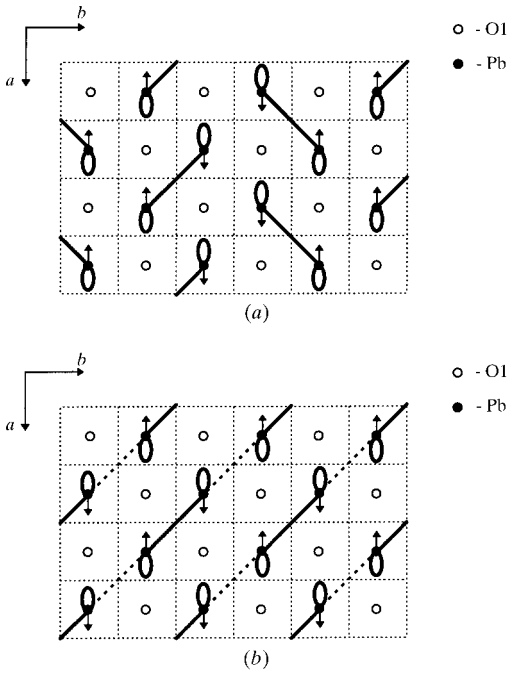

Fig. 12. Directions of displacements of Pb ions belonging to two neighboring Pb_2O_4 clusters and the space left behind (*a*) in the AFE-I structure and (*b*) in the AFE-II structure. A thin solid line connects Pb atoms in a Pb_2O_4 cluster. The dotted line connects Pb atoms in a high-energy configuration. Open circles represent axial O atoms and equatorial O atoms (not shown) lie in the corners of the grid. Arrows represent the directions of the Pb displacements (*a*) in the low-temperature AFE-I phase and (*b*) in the intermediate AFE-II phase.

Our observation that the local structure changes little through the antiferroelectric-to-paraelectric phase transition, T_c, suggests that the high-temperature paraelectric phase is locally and dynamically polarized with atoms seldom in their idealized cubic positions. The PDF refinement showed that Pb atoms were dynamically displaced along $[1\bar{1}1]$. What changes through T_c is the correlation among the displacements, from long-range correlation below T_c to short-range or no correlation above. This is a typical situation with the order/disorder transition. It is possible that the off-centering of Pb in the O_{12} cage is chemically driven by the lone-pair electrons, while the ferroelectricity is brought about by the interaction among the local polarizations. The local polarization of the PbO_{12} cluster is directly observable only by the PDF, but not in the reciprocal-space analysis; rather it leads to anomalously large thermal factors being refined in the Rietveld analysis.

6. Conclusions

The atomic structure of lead zirconate (PZ) was studied using the Rietveld refinement and the atomic pair distribution function analysis of pulsed neutron powder diffraction data in the temperature range 20–523 K. As expected, no difference was found between the local structure and the average structure of PZ at low temperatures. However, at elevated temperatures differences between the local and average structures developed owing to thermally excited atomic displacements. Interestingly, it is the long-range structure that changes most remarkably with temperature rather than the local structure. While PZ undergoes displacive transformations, the local atomic structure remains largely unchanged, even in the high-temperature cubic phase. Apparently the same atomic clusters arrange themselves in various patterns forming different long-range structures.

At all temperatures the Pb atom favors a particular local atomic arrangement which may repeat in different patterns, resulting in different long-range structures. The low-temperature antiferroelectric pattern (AFE-I) has been known for some time, but for the first time we have observed another type of in-plane Pb antiferroelectric ordering (AFE-II) in the intermediate phase, which gives rise to the $\frac{1}{2}\{110\}$ superlattice peaks. The evolution of the pattern from AFE-I to AFE-II develops gradually with increasing temperature and involves flipping of Pb displacements between the two equivalent local atomic arrangements. Since the intermediate phase exists over a very narrow temperature range, extensive local structural fluctuations would exist in the form of many nanodomains of the low-temperature AFE-I structure. This

explains why the crystallographic analysis which describes the volume average of the atomic positions does a poor job in describing the atomic structure of the intermediate phase. With the further increase in temperature Pb atoms randomly flip between equivalent local atomic arrangements. The high-temperature paraelectric phase is locally and dynamically polarized with atoms seldom in their idealized cubic positions. The displacements are not correlated from site to site and, therefore, are not directly observable in the reciprocal-space analysis; rather they lead to anomalously large thermal factors refined in the Rietveld analysis.

For the FE perovskites in general, covalent bonding between the cation and oxygen is essential in weakening the short-range repulsions and allowing the FE transition to occur (Cohen, 1992; Egami *et al.*, 1993). However, the size of the Zr^{4+} cation is rather large, with an ionic radius of 0.72 Å compared with 0.60 Å for Ti^{4+} (Shannon, 1976), to fit comfortably within the ZrO_6 cage. In PZ, apparently, the penalty of the local elastic energy within the ZrO_6 cage is too large for ferroelectricity to occur and no FE Zr displacement is observed.

On the other hand, it is recognized that the orbital hybridization of Pb and O forming a covalent bond enhances ferroelectricity in the Pb-based ferroelectrics such as $PbTiO_3$ (Cohen, 1992; Megaw, 1954). Our investigation suggests that even in PZ, the role of Pb off-centering due to the formation of Pb—O covalent bonds is very important. In PZ Pb ions are locally displaced, even at temperatures well above the AFE transition temperature, and the correlation among Pb displacements determines the long-range structure and dielectric properties of PZ. These considerations may be of special relevance for Pb-based relaxor ferroelectrics, such as $(Pb_{1-x}La_x)(Zr_{1-y}Ti_y)O_3$ (PLZT), the end member of which, PZ, is analyzed here, and $Pb(Mg_{1/3}Nb_{2/3})O_3$ (PMN). Indeed, the relaxor ferroelectrics are characterized with very diffuse phase transitions and a local polarization exists even at much higher temperatures (Burns & Docal, 1983).

Finally, the present study demonstrates that atomic PDF analysis can be more accurate than Rietveld refinement in determining the atomic positions and the thermal factors of a perfectly periodic crystalline structure. It also suggests that the PDF is a powerful method for studying crystal structure at finite temperatures since differences can develop between the local structure and the long-range structure as a result of thermal excitation.

The authors gratefully thank Professor Dwight Viehland for providing the sample and useful discussion. They also thank Drs R. E. Cohen, D. J. Singh and K. Rabe for informative discussion. They also acknowledge Simine Short for assistance in the powder neutron diffraction measurements. The Intense Pulsed Neutron Source is operated as a user facility by the US Department of Energy, Division of Materials Science, under contract W-31-109-Eng-38. Work at the University of Pennsylvania was supported by the Office of Naval Research through N00014-91-J-1036.

References

Billinge, S. J. L. (1992). PhD thesis, University of Pennsylvania, USA.
Burns, G. & Docal, F. (1983). *Solid State Commun.* **48**, 853–856.
Cochran, W. & Zia, A. (1968). *Phys. Status Solidi*, **25**, 273–283.
Cohen, R. E. (1992). *Nature*, **358**, 136–138.
Dai, X., Li, J.-F. & Viehland, D. (1995). *Phys. Rev. B*, **51**, 2651–2655.
Egami, T. (1995). *J. Phys. Chem. Solids*, **56**, 1407–1413.
Egami, T., Ishihara, S. & Tachiki, M. (1993). *Science*, **243**, 1307–1310.
Fujishita, H. & Hoshino, S. (1984). *J. Phys. Soc. Jpn*, **53**, 226–233.
Fujishita, H., Shiozaki, Y., Achiwa, N. & Sawaguchi, E. (1982). *J. Phys. Soc. Jpn*, **51**, 3583–3591.
Glazer, A. M. (1975). *Acta Cryst.* A**31**, 756–762.
Glazer, A. M. & Mabud, S. A. (1978). *Acta Cryst.* B**34**, 1060–1070.
Glazer, A. M., Roleder, K. & Dec, J. (1993). *Acta Cryst.* B**49**, 846–852.
Goulpeau, L. (1966). *Sov. Phys. Solid State*, **8**, 1970–1971.
Jona, F., Shirane, G., Mazzi, F. & Pepinsky, R. (1951). *Phys. Rev.* **105**, 849–850.
Jorgensen, J. D., Faber, J. J., Carpenter, J. M., Crawford, R. K., Haumann, J. R., Hitterman, R. L., Kleb, R., Ostrowski, G. E., Rotella, F. J. & Worton, T. G. (1989). *J. Appl. Cryst.* **22**, 321–333.
Kay, M. J. (1961). *Acta Cryst.* **14**, 80–81.
Leciejewicz, J. (1961). *Acta Cryst.* **14**, 1304.
McQueeney, R. J. & Egami, T. (1998). Unpublished.
Megaw, H. D. (1954). *Acta Cryst.* **7**, 187–194.
Perry, C. H., McCarthy, D. J. & Rupprecht, G. (1965). *Phys. Rev. A*, **138**, 1537–1538.
Roberts, S. (1949). *Phys. Rev.* **76**, 1215–1220.
Roleder, K., Kuegel, G., Handarek, J., Fontana, M. D., Carabatos, C., Hafid, M. & Kania, A. (1988). *Ferroelectrics*, **80**, 161–165.
Scott, B. A. & Burns, G. (1972). *J. Am. Ceram. Soc.* **55**, 331–333.
Shannon, R. D. (1976). *Acta Cryst.* A**32**, 751–767.
Shirane, G., Sawaguchi, E. & Takagi, Y. (1951). *Phys. Rev.* **84**, 476–481.
Singh, D. (1995). *Phys. Rev. B*, **52**, 12559–12563.
Slater, J. C. (1950). *Phys. Rev.* **78**, 748–761.
Stern, E. A. & Yacoby, Y. (1996). *J. Phys. Chem. Solids*, **57**, 1449–1455.
Tanaka, M., Saito, R. & Tsuzuki, K. (1982*a*). *J. Phys. Soc. Jpn*, **51**, 2635–2640.
Tanaka, M., Saito, R. & Tsuzuki, K. (1982*b*). *Jpn. J. Appl. Phys.* **21**, 291–298.
Tennery, V. J. (1966). *J. Am. Ceram. Soc.* **49**, 483–486.
Toby, B. H. & Egami, T. (1992). *Acta Cryst.* A**48**, 336–346.
Viehland, D. (1995). *Phys. Rev. B*, **52**, 778–791.
Von Dreele, R. B., Jorgensen, J. D. & Windsor, C. G. (1982). *J. Appl. Cryst.* **15**, 581–589.
Whatmore, R. W. & Glazer, A. M. (1979). *J. Phys. C*, **12**, 1505–1519.